Journal of Building Engineering 84 (2024) 108643

Contents lists available at ScienceDirect

Journal of Building Engineering

journal homepage: www.elsevier.com/locate/jobe

Full length article

Multiscale cracking pattern-based homogenization model of water permeability in hybrid fiber-reinforced concrete after high-temperature exposure

Lei Shen [a,*], Li Zhang [a], Xiang Yang [a], Giovanni Di Luzio [b], Lei Xu [a], Huimin Wang [a], Maosen Cao [c]

[a] Hohai University, College of Water Conservancy and Hydropower Engineering, Nanjing, 210098, China
[b] Politecnico di Milano, Department of Civil and Environmental Engineering, Milan, 20133, Italy
[c] Hohai University, Department of Engineering Mechanics, Nanjing, 210098, China

ARTICLE INFO

Keywords:
Water permeability
Multi-scale homogenization model
Steel fiber
Fine polyPropylene fiber
High temperatures

ABSTRACT

Hybrid steel-fine polypropylene fiber-reinforced concrete (HSPFRC) can effectively prevent thermal spalling. Its permeability at high temperatures plays a crucial role in avoiding spalling, and varies with the type, dosage, and length of fibers utilized in concrete mix. In this study, the water permeability of eleven different HSPFRCs after five different heating treatments is experimentally measured with a flow path representative of the material heterogeneity. Addition to the knowledge of the PP fiber tunnels around 150 °C, it is newly found that the thermal cracks caused by aggregate thermal expansion, instead of the evaporated PP tunnels and steel fiber induced thermal cracks, contributes the main part of water transport system over 150 °C. Steel fiber in SFRCs significantly reduces permeability by a factor of 10 through bridging forces that lessen the damage before reaching a temperature of 300 °C. However, after getting this temperature, permeability increases significantly by a factor of 10^4. For PFRCs, the permeability increases by a factor of 10^2 at 150 °C and continues to grow with the increase of fiber content and length. HSPFRCs exhibit similar patterns to PFRCs in terms of permeability. As the main innovation of this work, a multi-scale cracking pattern-based homogenization model for permeability in HSPFRC during and after high-temperature exposure is formulated and calibrated based on the experiments conducted in this research and validated using results from other tests.

1. Introduction

When concrete is exposed to high temperatures, it can experience thermal spalling due to a build-up of pore pressure and the presence of thermal stress [1–5]. To prevent spalling, two strategies have been found effective: adding steel fiber to improve concrete's bearing capacity, [6,7] and adding fine polypropylene (PP) fiber to increase permeability at high temperatures and limit pore pressure build-up [8–11]. Recent research has focused on studying the transport properties of hybrid steel-PP fiber-reinforced concrete (HSPFRC) exposed to high temperatures. Still, more research is needed to understand water permeability mechanisms and predict pore pressure in HSPFRC. Currently, no theoretical model exists for predicting water permeability in HSPFRC at high temperatures [12].

* Corresponding author.
E-mail addresses: shenl@hhu.edu.cn (L. Shen), leixu@hhu.edu.cn (L. Xu).

https://doi.org/10.1016/j.jobe.2024.108643
Received 5 October 2023; Received in revised form 20 January 2024; Accepted 24 January 2024
Available online 1 February 2024

PP fibers are frequently used to reduce pore pressure in concrete exposed to high temperatures due to their ability to increase water permeability at higher temperatures. In their works, Bošnjak et al. [13] introduced a novel testing configuration for assessing permeability in high-performance concrete, both with and without PP fibers, across temperatures ranging from 20 °C to 300 °C. Adding 1 kg/m^3 of PP fiber to concrete led to a sudden increase in permeability between 80 °C and 130 °C. The authors also highlighted the existence of pressure relief mechanisms beyond fiber melting based on their permeability measurements and SEM observations. Although the melting and burnout of fibers had a relatively small effect on pore volume, micro-cracks at high temperatures and the presence of PP fiber were found to increase the permeability [14]. Another study by Li et al. [10] focused on the effect of geometry and fraction of PP fiber on the permeability of ultra-high performance concrete (UHPC) subjected to elevated temperature. The study found that increasing fiber length and dosage, rather than fiber diameter, had a strong increasing effect on residual permeability due to the enhancement of fiber tunnel percolation. Zhang et al. [15] concluded that the thermal expansion of polymer fibers created microcracks even before fiber melting, which significantly increased permeability. Noumowe et al. [16] reported that at a higher temperature level of 600 °C, the air permeability of PFRC with 0.2% 13 mm length PP fiber in volume increased about 3000 times.

Adding a combination of steel and PP fiber to concrete is often used to prevent thermal spalling while maintaining mechanical resistance due to the fact that adding fine PP fiber can lower its mechanical strength [17–20]. HSPFRC's water permeability has only been studied preliminarily compared to PFRC. Studies by Algourdin et al. [21] and Yermak et al. [22] have shown that CPPS 0.75–60 concrete (HSPFRC with 0.75 kg/m^3 PP fiber and 60 kg/m^3 steel fiber) has higher porosity and permeability values than plain concrete at temperatures between 200 °C and 300 °C. The permeability of plain concrete, SFRC, and HSPFRC increases about 21, 38, and 85 times at 300 °C, respectively. Suhaendi et al. [23] conducted experiments to examine how 6 mm-long PP fibers affect the residual water permeability of heated high-strength concrete. Their findings showed that the HSPFRC with 0.25% short PP fibers and 0.5% steel fiber increased 26 times when heated up to 400 °C, while the HSPFRC with the same amount of PP fibers and steel fiber increased 1168 times. This study highlights that steel fiber can reduce residual water permeability at temperatures below 400 °C. Meanwhile, Li et al. [24] found that adding PP fibers or larger aggregates significantly increased hot permeability below 300 °C, while steel fiber did not contribute to its increment. This effect was mainly attributed to the formation of interconnected micro-crack networks at elevated temperatures.

There are still three aspects of the experimental studies mentioned above that need further analysis. Firstly, the distance at which air or water permeability has been typically measured along the flow path is smaller than the size of a representative volume element, which is roughly three times the maximum size of aggregates or fibers. Bošnjak et al. [13] and Suhaendi et al. [23] used the RILEM-CEMBUREAU method with 100 mm diameter cylinder specimens. Their water flow distance did not exceed 50 mm, while the maximum aggregate diameter and maximum fiber length were 20 mm and 30 mm, respectively. Li et al. [10,24] used the standard testing method ASTM C1437 [25], whose airflow distance is 50 mm, using HSPFRCs with aggregates of maximum size 5 mm, steel fibers of length 13 mm, and PP fibers of length 12 mm. Secondly, it is important to note that the high-temperature range for this material is limited to temperatures below 400 °C, which means it may not be suitable for use in extremely high-temperature environments such as fires. Furthermore, the impact of the amount and length of PP fibers on the water transport capabilities of HSPFRC was not taken into account.

In the literature, there are few studies with reasonable micro- and mesoscale explanations and prediction models about the evolution of permeability at different temperatures on a macro-scale. Li et al. [10] used a mixed parallel-series model to predict the hot air permeability of PP fiber-reinforced UHPC by fitting experimental data. This empirical model needs recalibration when there are changes in aggregate size and fiber geometry. It has been observed through experiments [26] and simulations [27,28] that cracks significantly affect the permeability of concrete. During heating, thermal cracks [29–31] are the most common form of damage. Therefore, it is necessary to consider the thermal cracking pattern at the micro/mesoscale. Therefore, predicting the individual and combined effects of steel and fine PP fibers on concrete permeability at and after high temperatures is very challenging. A model was previously developed by Wang et al. [32] for predicting the permeability of Engineered Cementitious Composites at ambient temperature by incorporating PP fibers. Their model utilized the General Effective Media Theory (GEM) [33] to predict cement paste permeability, the General Self-Consistent Scheme [34] for matrix permeability, and a parallel model for predicting permeability of PP fiber reinforced cementitious composites. Baji et al. [35] also presented an analytical model for predicting concrete permeability while accounting for Interfacial Transient Zone (ITZ) flow due to aggregate inclusion. This model was later simplified as a fitting function to predict permeability variations due to ITZ flow [36], which was employed to predict the permeability of concrete with thermal cracks caused by high-temperature treatments [29,30]. Hence, a multiscale theoretical model is necessary to accurately predict the permeability of high-strength performance fiber-reinforced concrete (HSPFRC) at high temperatures due to its complex material structure and cracking patterns.

The purpose of this research is to explore the water permeability characteristics of plain concrete, SFRC, PFRC, and HSPFRC after being exposed to high-temperature treatments. In Section 2.1, a detailed experiment is carried out to analyze the effects of steel fiber dosage, PP fiber dosage, and PP fiber length on water permeability using experimental techniques. In Section 2.2, we introduce a novel multiscale homogenization model for thermally damaged HSPFRC. The model takes into account the impact of high-temperature exposure, coarse aggregate dosage, steel fiber dosage, PP fiber dosage, and PP fiber length. It is worth mentioning that the proposed model only requires information on the mixture composition and porosity measured at different temperatures as input. The comparison between the experimental data and model predictions is discussed in Section 3 with their mechanisms, while the validation of the model is explained in Section 4.

Table 1
Concrete mix in the experiment (Unit: kg per 1/m^3 concrete).

Mix label	Cement	Water	Fine Agg.	Coarse Agg.	Superplasticizer	Steel fiber	PP fiber
S0P0	500	150	713	1027	13.5	0	0
S0P1L12	500	150	713	1027	13.5	0	0.91
S0P2L6	500	150	713	1027	13.5	0	1.82
S0P2L12	500	150	713	1027	13.5	0	1.82
S0P2L19	500	150	713	1027	13.5	0	1.82
S1P0	500	150	713	1000	13.5	79	0
S1P1L12	500	150	713	1000	13.5	79	0.91
S1P2L6	500	150	713	1000	13.5	79	1.82
S1P2L12	500	150	713	1000	13.5	79	1.82
S1P2L19	500	150	713	1000	13.5	79	1.82
S2P0	500	150	713	1000	13.5	158	0

2. Methods

2.1. Experimental investigation

2.1.1. Mix proportions and test specimens

Eleven different types of concrete, including plain high-strength concrete (HSC), steel fiber-reinforced concrete (SFRC), PP fiber-reinforced concrete (PFRC), and hybrid steel-PP fiber-reinforced concrete (HSPFRC), underwent a comprehensive test program to assess their water permeability and porosity.

All the mixes comprise ordinary Portland cement 42.5, polycarboxylate superplasticizer of DYS881-PZ (Chinese Standard GB8076-2008), crushed limestone as coarse aggregates with a maximum diameter of 20 mm and a minimum diameter of 5 mm, along with natural river sand as fine aggregate. The mixture details are presented in Table 1. Each mixture is labeled with a code indicating the type and volume of fibers used. The label Sn refers to a mix containing steel fibers with a volume fraction of n%, Pn refers to a mix containing PP fibers with a volume fraction of n‰, and Lx indicates the length of the PP fibers in millimeters. The fiber-reinforced concrete mixes meet the requirements of the Chinese technical specification for fiber-reinforced concrete structures (CECS 38:2004) and contain commercially available fibers in China, including two ends hooked steel fibers and monofilament PP fibers. The steel fibers are 30 mm in length and 0.55 mm in diameter, giving them an aspect ratio of 54.5. They have a high melting temperature of 1500 °C. The nonabsorbent PP fibers, on the other hand, have a melting temperature of 165 °C and come in three different lengths: 6 mm, 12 mm, and 19 mm. They have an equivalent diameter of 48 μm.

For our experiment, we produced 55 cylindrical specimens that were 200 mm long and 100 mm in diameter. Once they were cast, we left them in the molds for 24 h before removing them. Then, we cured them under standard conditions in a room with a relative humidity of at least 95% and a temperature of 20 ± 2 °C for 28 days.

2.1.2. Test procedure and apparatus

After five heating treatments, we tested the 55 cylinder specimens to gather data on water permeability and porosity (Fig. 1(a)). We used a computer-controlled electric furnace that reaches up to 1200 °C with a maximum heating rate of 30 °C/min for the thermal treatments. We considered 5 target temperatures, namely 60 °C, 150 °C, 300 °C, 450 °C and 600 °C, applying a heating rate of 5 °C/min. After heating, we kept the specimens at the target temperatures for three hours and then allowed them to cool naturally in the furnace for 24 h. All heating treatments were performed when the concrete was 65 days old.

To conduct the porosity tests, the ASTM cold water saturation technique was utilized [31]. The specimens underwent heating in the oven at 60 °C, 150 °C, 300 °C, 450 °C and 600 °C to determine the oven dry mass (W_d). Afterward, they were put in water at around 20 °C for 72 h to determine the saturated surface-dry mass (W_s) and the buoyant mass (W_b). The permeable porosity (ϕ_{cap}) of HSPFRC can be calculated by considering the weight increase due to water absorption and the weight reduction caused by buoyancy, which can be expressed as:

$$\phi_{cap} = \left(W_s - W_d\right) / \left(W_s - W_b\right) \tag{1}$$

Capillary porosity in concrete refers to the interconnected network of small pores that allows the ingress and movement of water through the material. The evolution of capillary porosity over time in concrete is influenced by many factors, such as the curing conditions, water-to-cement ratio, cement type, supplementary cementitious materials, environmental exposure, etc. [37]. Over time, capillary porosity decreases as hydration products, such as calcium silicate hydrate (C–S–H) gel, fill the voids. The microstructure becomes more refined with continued hydration, which results in a reduction in capillary porosity. This reduction continues with time, although at a slower rate compared to the earlier stages [38]. The ongoing hydration and formation of additional hydration products lead to the densification of the cementitious matrix [39].

The water permeability of all 55 specimens was measured using the multi-physics seepage test apparatus designed and manufactured by the Seepage Lab at Hohai University. The apparatus is shown in Fig. 1(b). The equipment is managed by a central computer that oversees the axial load system, seepage load system, confinement load system, and temperature control system. The maximum axial load is 1500 kN, while the maximum confinement pressure and seepage pressure are 30 MPa and 15 MPa,

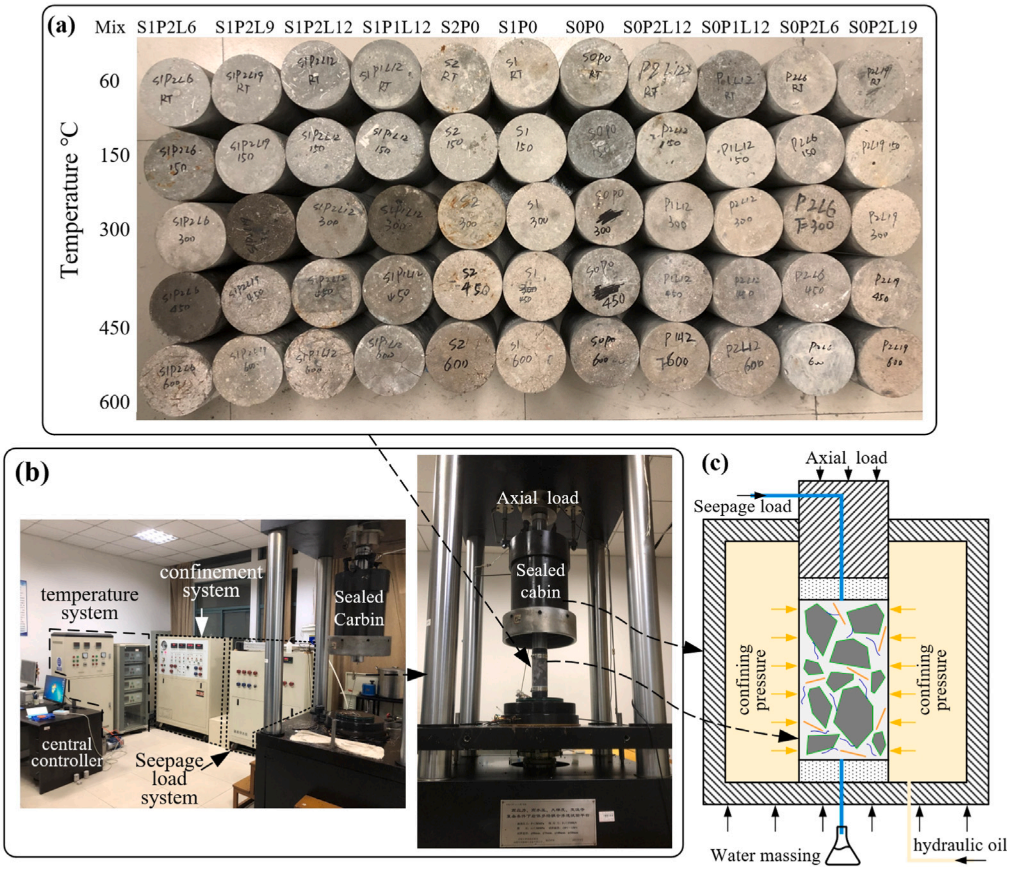

Fig. 1. Experimental setup: (a) Specimens after heating treatments; (b) apparatus in water permeability test, and its (c) illustration.

respectively. The temperature range is between −15 °C and 150 °C. For the research conducted, the axial load was set to 20 kN (≈10 MPa) to secure the specimen, and a confinement pressure of 1.5 MPa was used, which is higher than the applied hydraulic pressure of 1 MPa, denoted as p_w. All tests were carried out at room temperature. The hydraulic pressure was applied on the top of the confined specimen, and the amount of water that exited from the bottom was measured. From the measured water mass, the volumetric flow (Q_w) was calculated, as shown in Fig. 1(c).

Darcy's law describes the one-dimension laminar flow in a porous material which refers to the test set-up can be expressed as:

$$Q_w = -\kappa \frac{A}{\eta_w} \frac{p_w}{L} \tag{2}$$

where Q_w [m^3/s] is the volumetric flow, k [m^2] is the permeability of the medium, $A = \pi D^2/4$ [m^2] is the area of the specimen perpendicular to the flow direction, p_w [Pa] is the pressure difference, L is the specimen height, and η_w [Pa·s] is the water dynamic viscosity of the permeating fluid. Intrinsic permeability describes the ability of a porous material to resist fluid ingress and depends only on the geometry and connectivity of the porous network. For incompressible fluids, such as water, the permeability k in Eq. (2) corresponds to the intrinsic permeability, which is not true for compressible fluids. In this study, we define the water permeability as $k_T^{mix} = \kappa_T^{mix} \rho_w g / \eta_w$ [m/s] with each mix (superscript mix) and temperature (subscript T), which can be directly obtained from the experimental measurement. The water permeability tests start at the concrete age of 75 days and last for four months since the tests for specimens without heating treatments usually take seven days.

2.2. Multiscale homogenization model

This section proposes a multiscale cracking pattern-based homogenization model for evaluating permeability in FRC with and without high-temperature treatment. The proposed model can physically bridge the gap between the mesoscopic ($10^{-4} \sim 10^{-1}$ m) and the macroscopic ($1 \sim 10^{-1}$ m) mass transport behavior. The proposed model computes the impact of high temperatures on the permeability, considering the pore structure variation, i.e., porosity and pore connectivity increase. One of the main innovations of the proposed model is that the permeable porosity and pore connectivity are derived based on the mesoscopic material-structure variations caused by high temperatures rather than using some mathematical functions to express the temperature dependence of

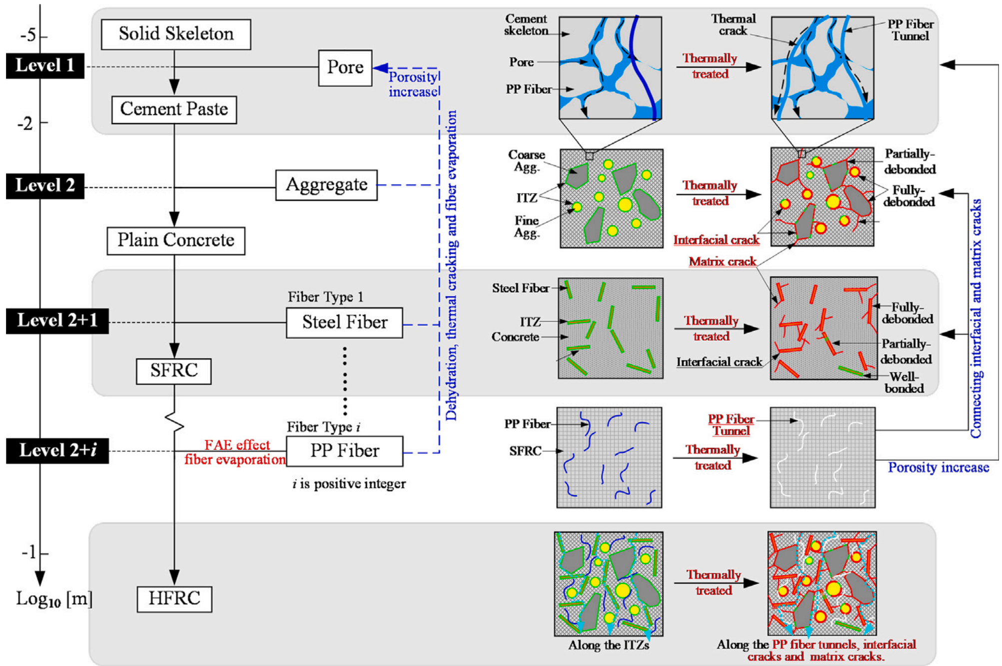

Fig. 2. Illustrations of the multiscale model.

the different components at the mesoscale. This multiscale homogenization model is presented step by step in the following sections and illustrated in the flowchart of Fig. 2.

Level 1: Cement paste = solid skeleton + pore

In the first level of the homogenization procedure in Fig. 2, we consider the cement paste as the porous media made up of the solid skeleton and the pores. The permeability of this porous media, such as hardened cement paste, mainly depends on the overall porosity and the pore connectivity. To derive the effective water permeability of cement paste, the general effective media (GEM) equation [32–34] can be employed. The GEM equation [32,33] for the flow of water in a porous medium can be written as:

$$\frac{\left(1-\phi_{cap}\right)\left(k_{sld}^{1/\beta}-k_{paste}^{1/\beta}\right)}{k_{sld}^{1/\beta}+Bk_{paste}^{1/\beta}}+\frac{\phi_{cap}\left(k_{por}^{1/\beta}-k_{paste}^{1/\beta}\right)}{k_{por}^{1/\beta}+Bk_{paste}^{1/\beta}}=0 \quad \text{with} \quad B=\frac{1-\phi_{cri}}{\phi_{cri}} \tag{3}$$

where k_{por} is the permeability of pores in cement paste [m^2], k_{sld} is the permeability of solid skeleton in cement paste [m^2], ϕ_{cap} is experimental measured capillary porosity, and ϕ_{cri} is the critical porosity that the pore network first percolates.

The analytic solution to Eq. (3) can be derived in terms of the normalized permeability, which is expressed as:

$$\frac{k_{paste}}{k_{sld}}=\left[A+\sqrt{A^2+B\left(\frac{k_{por}}{k_{sld}}\right)^{1/\beta}}\right]^{\beta} \tag{4}$$

with:

$$A\left(\phi_{cap}\right)=\frac{1}{2}\left\{\left(\frac{k_{por}}{k_{sld}}\right)^{1/\beta}+\frac{\phi_{cap}}{1-\phi_{cri}}\left[1-\left(\frac{k_{por}}{k_{sld}}\right)^{1/\beta}\right]-B\right\} \tag{5}$$

The critical porosity, ϕ_{cri}, is here computed considering the effect of the PP at high temperatures through the temperature-dependent volume fraction of PP fiber (V_{PF}) as:

$$\phi_{cri}(T)=0.17-\alpha_{PF}(T)V_{PF} \tag{6}$$

where V_{PF} is the initial PP volume fraction and α_{PF} is coefficient that represents the state of PP fiber at the temperature T [°C] as:

$$\alpha_{PF}(T)=\frac{\left\langle \min\left(T,T_{vend}\right)-T_{melt}\right\rangle}{T_{vend}-T_{melt}} \tag{7}$$

in which, T_{melt} = 165 °C is the start temperature of PP melting, and T_{vend} = 475 °C is the end temperature of PP vaporization. According to the Eq. (7), $\alpha_{PF}=0$ represents fully evaporated PP fibers, $\alpha_{PF}=1$ represents PP fibers in solid state, $0<\alpha_{PF}<1$ represents PP fibers in soft/liquid state.

To characterize the pore structure, the coefficient, $\beta(T, V_{PF}, L_{PF})$, is introduced which represents the level of pore connectivity. The pore connectivity increases with the temperature, the volume fraction of PP fibers and the length of PP fibers, which can be expressed as:

$$\beta\left(T, V_{PF}, L_{PF}\right) = 2.7 - \frac{T}{1000} - \left(1 - \alpha_{PF}\right) \frac{V_{PF}}{0.01} \frac{L_{PF}}{0.12} \tag{8}$$

where L_{PF} is the initial length of the PP fibers.

The permeability in the pores can be characterized by the Katz and Thompson equation [33,40] that expresses the permeability of a porous cement paste as:

$$k_{por} = \frac{1.8}{226} r_{cri}^2 \left(1 - \phi_{cri}\right)^2 \tag{9}$$

where r_{cri} is the critical radius of the capillary pores measured via mercury intrusion porosimetry (MIP) and the critical radius increases with the temperature. The initial value approximates 0.055 μm for 35 days old cement paste with water-binder ratio (W/C) of 0.3 [33] and increase from 0.055 μm to 5.5 μm for the concrete with $W/C = 0.26$ after exposure to 600 °C [41]. Thus, interpolating between those values a linear relationship for r_{cri} [μm] vs T [°C] is here proposed as:

$$r_{cri} = \frac{5.5 - 0.055}{600 - 20} (T - 20) + 0.055 \tag{10}$$

The solid skeleton of cement paste typically consists of three main components: Calcium–Silicate–Hydrates (CSH) gel, portlandite (CH), and unhydrated (UH) cement particles. Among them, only CSH gel is permeable, and the others can be considered impermeable. For this material the GEM theory can be applied to calculate the overall permeability, in which the CSH gel is the high-permeable phase ($k_{CSH} > 0$), and CH and unhydrated cement particles are the low-permeable (impermeable phase, i.e. $k_0 \approx 0$). Therefore the overall permeability of the cement paste solid skeleton is given by:

$$k_{sld} = k_0 \left(1 - \phi_{CSH}\right) + k_{CSH} \phi_{CSH} \left(1 - \frac{1 - \phi_{CSH}}{1 - \phi_c^{CSH}}\right)^2 \tag{11}$$

where the CSH gel permeability $k_{CSH} = \kappa_{CSH} \cdot \rho_w g / \eta_w = 7 \times 10^{-16}$ [m/s] ($\kappa_{CSH} = 7 \times 10^{-23}$ [m^2] [42] and $\eta_w = 1.01 \times 10^{-3}$ [Pa · s]), the critical volume fraction of CSH $\phi_{cri}^{CSH} = 0.17$ [33], and ϕ_{CSH} is the volume fraction of CSH gel in the solid phase, which can be calculated as:

$$\phi_{CSH} = \frac{V_{CSH}}{V_{unhyd} + V_{hyd}} \tag{12}$$

where V_{unhyd} is the volume fraction of unhydration products and V_{hyd} is the volume fraction of hydrated cement particles (CSH and CH). The volume fraction of hydration products can be calculated by adopting the Power's model [43]. For ordinary Portland cement paste we have:

$$V_{unhyd} = \frac{0.68 \alpha_{hyd}}{(W/C) + 0.32} \tag{13}$$

$$V_{hyd} = V_{CSH} + V_{CH} = \frac{0.32 \left(1 - \alpha_{hyd}\right)}{(W/C) + 0.32} \tag{14}$$

where the volume ratio V_{CSH}/V_{CH} is 1.66/0.63 [44] and $\alpha_{hyd}(T)$ is the cement hydration degree. The initial hydration degree can also be calculated from Power's model [43], if the capillary porosity of cement paste is known.

$$\alpha_{hyd}(20) = \frac{\left[1 - \phi_{cap}(20)\right] (W/C) - 0.32 \phi_{cap}(20)}{0.36} \tag{15}$$

where W and C are the water and cement mass per unit volume concrete, respectively. Hence, $\alpha_{hyd}(20)$ can be computed with $W/C = 0.3$ (Table 1) and a porosity of 0.015 at room temperature (Table 2), which yields $\alpha_{hyd} = 0.8075$. Unfortunately, the experimental campaign did not provide calorimetry, loss on ignition, and electrical resistivity measurements, which are more appropriate techniques for measuring hydration degree than the methods used here from the capillary porosity measurement. The effect of dehydration caused by high temperature is considered as a function that proposed by Gawin et al. [45] and calibrated by the experimental data [46,47].

$$\alpha_{hyd}(T) = \alpha_{hyd}(20) \left[1 - \sum_{i=1}^{3} b_i^c (T - 105)^i\right] \tag{16}$$

in which, $b_1^c = 4.6647 \times 10^{-3}$, $b_2^c = -7.8830 \times 10^{-6}$ and $b_3^c = 4.4485 \times 10^{-9}$ are empirical coefficients with unit 1/°C.

Level 2: Concrete = cement paste + aggregate

As we scale up to the second level of consideration in Fig. 2, we view concrete material as a two-phase composite consisting of cement paste (as the matrix phase) and aggregates (fine and coarse) as the inclusion phase. The aggregates are assumed to be impermeable, and their interfaces with cement paste, i.e., ITZ, generally have a permeability ranging from 1.3 to 16.2 times that of the cement paste. When impermeable inclusions are added to the cement paste matrix, the water flow in the ITZ increases, thereby increasing permeability. The ITZ is subject to interface cracks and damage due to mismatches of thermal strains between inclusions and matrix after high-temperature treatments. Consequently, water flow in the ITZ interface can significantly increase the overall permeability of concrete. Baji et al. [35,36] proposed a mathematical simplified analytical model, which here is improved to estimate thermally damaged concrete based on mesoscopic thermal cracking patterns. The model reads as follows:

$$\frac{k_{con}}{k_{paste}} = \left(1 - 1.4123V_{Agg} + 0.0227V_{Agg}^2\right) + 1.4665\left(1.6863V_{Agg} - V_{Agg}^2\right)\left(1.2\xi_{max} + \xi_{max}^2\right) \tag{17}$$

$$\xi_{max} = \frac{4k_{ITZ}\delta_{ITZ}}{k_{paste}d_{max}} \tag{18}$$

where $d_{max} = 25$ mm is the maximum diameter of aggregate and the $V_{Agg} = 0.62$ is the total volume fraction of fine and coarse aggregate. The ITZ thickness is assumed as 20 μm at ambient temperature (between 0 °C and 100 °C) [48] and increases above 100 °C with following the expression:

$$\delta_{ITZ}(T) = r_{ck}\delta_{ITZ}(20) \tag{19}$$

where r_{ck} is the ratio of the thermal crack opening over the ITZ thickness which is computed as:

$$r_{ck} = 4\log_2\left(1 + \frac{\langle T - 170\rangle}{100}\right) - \frac{V_{SF}}{0.02}\left(\frac{T - 240}{100}\right)^2 0^{V_{PF}} + \frac{\langle T - T_{melt}\rangle}{100}\frac{0.1}{0.48 + V_{PF}} \tag{20}$$

The equation on the right hand side consists of three terms. The first term has an initial value of 4 and increases as the temperature reaches 170 °C. This term is related to the interfacial thermal crack effect on aggregate interfacial cracking. The second term takes into account the effect of steel fiber on the aggregate interfacial cracking. It decreases with temperature below 240 °C due to the steel fiber bridging forces, but increases with temperature at higher temperatures due to thermal cracks caused by steel fiber expansion. This effect can be eliminated by adding fine PP fiber to the mix. The third term considers the effect of fine PP fiber on aggregate interfacial cracking. This term decreases with temperature and with the volume fraction of PP fibers. When PP fiber melts, it can partially prevent the damage caused by the pore pressure build-up at high temperatures.

By assuming that the water flow in the cracks postulates a Poiseuille diffusion and accounting for the influence of $Fiber\ Adhering\ Effect$ (FAE), the permeability ratio k_{ITZ}/k_{paste} can express function of the temperature and PP fiber content as:

$$\frac{k_{ITZ}(T)}{k_{paste}(T)} = \frac{k_{ITZ}(20)}{k_{cem}(20)}\left(r_{ck}^3 + \frac{V_{PF}}{0.001}r_{FAE}\right) \tag{21}$$

where r_{FAE} represents the increasing effect caused by the FAE of PP fiber. This term is defined as:

$$r_{FAE} = 500\left[\exp\left(\frac{\langle T - T_{vend}\rangle}{100}\right) - 1\right] + 200\frac{\langle T - T_{soft}\rangle}{|T - T_{soft}|}\left[1 + \frac{L_{PF}}{d_{max}}\left(\frac{L_{PF}}{0.012} - 1\right)\right] \tag{22}$$

The FAE takes effect when the PP fiber starts to soften ($T_{soft} = 100$ °C), and this phenomenon increases with the temperature and PP fiber length. After the PP fiber melting and evaporation, the FAE can still increase with temperature since the further development of thermal cracks can be better connected by tunnel voids left by PP fibers.

Level 3: SFRC = concrete + steel fiber

In the third level of the multi-scale scheme in Fig. 2, there are two phases: plain concrete and steel fibers. The steel fibers have a high melting point of 1200 °C and are considered impermeable inclusions. As a result, the ITZ interface flow dominates the permeability increase of SFRC due to a larger amount of the ITZ surface at ambient temperature and thermal cracks at high temperatures. To predict the permeability of SFRC with and without thermal damage, the general self-consistent scheme (GSCS) [49] is used. GSCS is an approximate method derived from the composite spheres assemblage (CSA) model proposed by Hashin [49]. The simple models developed by Hashin for the conduction in a composite with imperfect interfaces between matrix and particle inclusions were later extended to diffusion [34]. Using this approach, the permeability of a matrix with impermeable inclusions of various shapes can be expressed as:

$$\frac{k_{SFRC}}{k_{con}} = 1 + \frac{V_{SF}}{\frac{1-V_{SF}}{n_{SF}} + \frac{1}{\left(\frac{k_{ITZ}(T)}{k_{con}}\right)\left(\frac{\delta_{ITZ}(T)}{d_{SF}}\right) - 1}} \tag{23}$$

where $k_{ITZ}(T)$ and $k_{con}(T)$ are the permeability of ITZ and concrete, respectively; $\xi_{ITZ}(T)$ is the thickness of ITZ between steel fibers and concrete; V_{SF} is the steel fiber total volume fraction in mix; n_{SF} is the shape coefficient of steel fiber which is defined by [50,51]:

$$n_{SF} = \frac{S_{SF}}{V_{SF}^{2/3}}\left(\frac{3}{4\pi}\right)^{1/3} \tag{24}$$

where the steel fibers are assumed as cylinders with length L_{SF} and diameter d_{SF}, and the S_{SF} and V_{SF} are the signal steel fiber surface area and volume, respectively. The shape coefficient $n_{SF} = 3$ as given in the CSA model proposed by Hashin [49] and $n_{SF} = 8.76$ when the inclusions are cylinders with a length of 30 mm and a diameter of 0.55 mm. The geometry parameters are temperature-independent since the steel fiber is stable up to 1200 °C. Hence the variation of ITZ thickness and the ratio of ITZ's permeability over concrete follow Eqs. (19) and (21), respectively.

Table 2
Porosity and permeability of the studied mixes.

Mix	20 °C		150 °C		300 °C		450 °C		600 °C	
	Prosoity [%]	permeability [m/s]	Prosoity [%]	permeability [m/s]	Prosoity [%]	permeability [m/s]	Prosoity [%]	permeability [m/s]	Prosoity [%]	permeability [m/s]
S0P0	1.50	1.25×10^{-10}	7.70	4.10×10^{-11}	11.86	7.83×10^{-09}	15.94	7.60×10^{-08}	17.29	3.46×10^{-07}
S1P0	2.05	1.29×10^{-10}	7.60	4.84×10^{-11}	11.34	2.02×10^{-09}	15.51	6.97×10^{-08}	17.91	7.75×10^{-07}
S2P0	1.91	9.81×10^{-11}	8.27	3.99×10^{-11}	11.46	2.02×10^{-10}	15.40	4.66×10^{-08}	17.67	4.34×10^{-07}
S0P1L12	1.49	9.44×10^{-11}	8.02	5.67×10^{-10}	11.32	2.38×10^{-09}	15.14	1.76×10^{-08}	17.13	2.67×10^{-07}
S0P2L12	2.00	9.44×10^{-11}	9.07	2.16×10^{-09}	11.05	4.86×10^{-09}	13.99	2.68×10^{-08}	18.42	6.32×10^{-07}
S0P2L6	1.67	6.23×10^{-11}	7.30	1.16×10^{-09}	10.76	4.02×10^{-09}	14.92	1.48×10^{-08}	16.36	3.99×10^{-07}
S0P2L19	1.82	1.89×10^{-10}	6.97	4.44×10^{-09}	10.89	9.96×10^{-09}	14.60	4.43×10^{-08}	15.85	9.61×10^{-07}
S1P1L12	1.80	9.44×10^{-11}	7.10	1.41×10^{-09}	11.10	4.67×10^{-09}	14.20	2.79×10^{-08}	17.00	1.14×10^{-07}
S1P2L12	1.64	9.44×10^{-11}	7.80	3.24×10^{-09}	10.30	1.21×10^{-08}	13.30	1.01×10^{-07}	15.80	3.93×10^{-07}
S1P2L6	1.53	1.23×10^{-10}	8.00	9.43×10^{-10}	11.30	4.86×10^{-09}	14.70	2.49×10^{-08}	16.70	4.72×10^{-07}
S1P2L19	1.60	1.51×10^{-10}	7.80	4.42×10^{-09}	11.20	1.57×10^{-08}	13.40	1.03×10^{-07}	15.90	8.12×10^{-07}

Table 3
Compression strength, thermal conductivity and pore pressure peak of the studied mixes.

Mix	Comp. strength [MPa]		Thermal conductivity W/(m · °C)		Pore pressure peak [°C]	[MPa]
	before	after	before	after	Peak Temp.	Peak pressure
S0P0	70.2	40.8	1.78	0.97	229.28	1.62
S1P0	90.2	45.6	1.88	1.04	223.56	1.17
S2P0	95.2	51.6	2.02	1.02	233.83	1.78
S0P2L6	69.1	39.4	1.76	0.88	217.74	0.99
S0P2L12	69.4	34.2	1.77	0.89	304.88	0.68
S0P2L19	69.5	34.5	1.75	0.88	184.7	0.63
S1P2L6	95.6	52.2	1.89	0.93	240.6	0.83
S1P2L12	95.0	47.4	1.89	0.98	241.72	1.1
S1P2L19	89.1	49.8	1.90	1.01	215.11	1.29

Level 4: HSPFRC = SFRC + fine PP fiber

In the last step of the homogenization procedure at the material scale in Fig. 2, the two phases are the SFRC as the matrix and the soft and fine PP fibers as inclusions. The PP fibers are considered impermeable inclusions at ambient temperature. Nevertheless, different from the steel fibers, the interface flow of PP fibers is ignored here since the PP fiber diameter of 48 μm is close to the ITZ thickness of 20 μm to 40 μm. Hence, the permeability of a matrix with impermeable PP fiber is derived from a simplified parallel model, which can be expressed as [32]:

$$\frac{k_{HSPFRC}}{k_{SFRC}} = 1 - \alpha_{PF} V_{PF} \tag{25}$$

in which, the α_{PF} is coefficient that represents the state of PP fiber at the temperature T [°C] as defined in Eq. (7). It is worth noting that the increasing effect of PP fiber on permeability over 165 °C is considered through three different features as illustrated in Fig. 2: (1) the decreasing of V_{PF} due to PP effects evaporation in this Level 4; (2) the tunnel effects in the matrix is considered at the Level 1 for cement paste; (3) the melting and evaporation of PP fibers that significantly increase the pore connectivity between thermal cracks induced by coarse aggregates and steel fibers in Level 2 and 3.

3. Results and discussion

3.1. Comprehensive properties of HSPFRC

Table 2 shows the water permeability and porosity measurements for all mixtures, both with and without heat treatment. The water permeability of plain concrete and SFRC showed a slight decrease when treated at 150 °C. However, the water permeability of the other 11 mixtures significantly increased with heating temperatures above 300 °C. This increase in permeability may be due to further hydration during heating treatment up to 150 °C. Additionally, this hydration caused slight increases in compression strengths of plain concrete and SFRC, as shown in Table 3. As reported in Table 2, the porosity of all mixtures increased with heating temperatures, but there was not much variation due to limited steel and PP fiber dosage in the mixes.

Previous experimental investigations have tested the cubic compression strength [7], thermal conductivities [31], and pore pressure build-up [52] of the same mixtures. Table 3 presents the data gathered from these tests and anyone interested in additional details can refer to the earlier works [7,31,52]. These data will be utilized to analyze the mesostructure variations of HSPFRC due to heating. This will result in a better understanding of the mechanisms responsible for the permeability variation of HSPFRC.

3.2. Influence of steel fiber content on plain concrete

Two levels of steel fiber dosage were considered, namely 1% (S1P0) and 2% (S2P0) of the volume fraction. The experimental measurements and model predictions (using Eq. (25) with $V_{PF} = 0$) for S1P0 and S2P0 are presented in Fig. 3. The results show

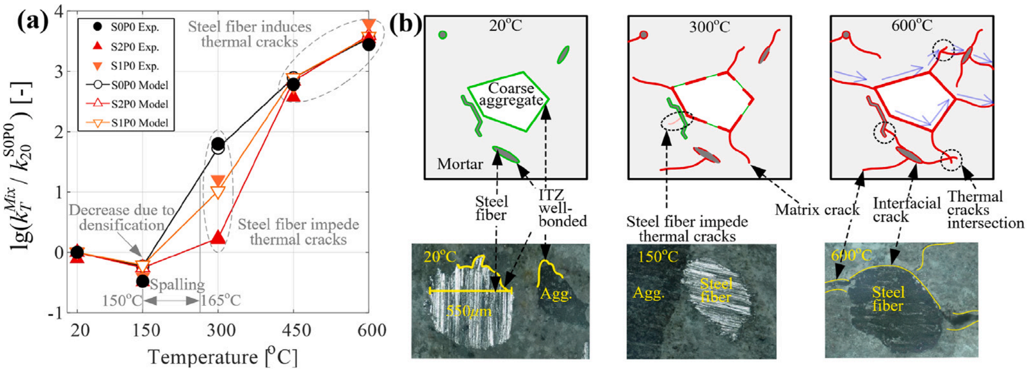

Fig. 3. Influence of steel fibers content: (a) Experimental data and model predictions; (b) mesoscale mechanisms.

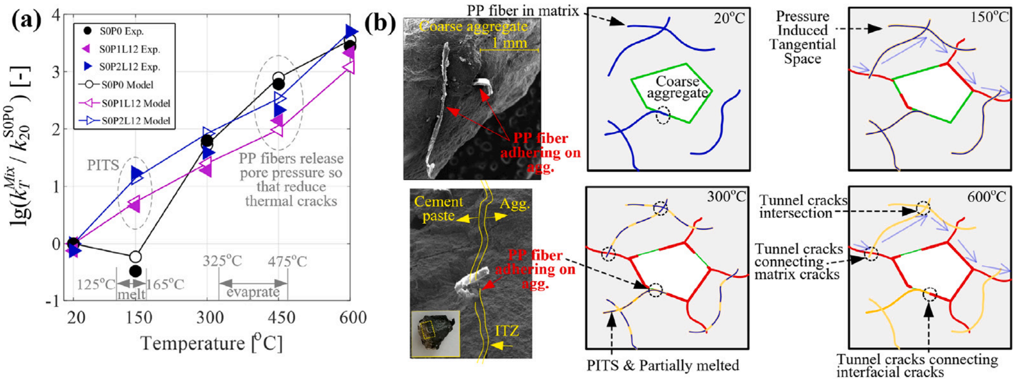

Fig. 4. Influence of PP fibers content on plain concrete: (a) experimental data and model predictions; (b) mesoscale mechanisms.

that as the temperature increases, the permeability of the concrete also increases, reaching values at 600 °C that are 10^3 to 10^4 times higher than the initial values at 20 °C, similar to those of plain concrete. However, the study found that the thermal cracks caused by steel fiber expansion have a minimal impact on the permeability compared to the cracks caused by the coarse aggregate. Interestingly, it was observed that the presence of steel fibers reduces the permeability below 450 °C, while it increases at 600 °C. Additionally, Fig. 3 shows a significant difference in permeability at 150 °C.

The reasons for the changes in permeability of SFRC after exposure to high temperatures can be attributed to the effects of steel fibers. There are two main effects that occur. Firstly, the permeability is reduced due to the increased internal cohesion caused by fiber bridging forces. This is shown in Fig. 3(b), where the steel fibers can sometimes be placed next to the coarse aggregates, which prevents the formation of thermal cracks induced by the aggregates within the temperature range of 150 °C to 450 °C. This effect is more pronounced at 150 °C because the permeability decreases by a factor of ten for each addition of 1% volume fraction of steel fibers. This mechanism can also explain the higher pore pressure peaks of SFRC reported in [52] and the higher spalling risk reported in [7]. Secondly, the permeability increases above 450 °C due to the rise effect. The water transport network primarily consists of thermal cracks generated by materials with higher thermal expansion coefficients (i.e., aggregates and steel fibers), as shown in Fig. 3(b). To some extent, these thermal cracks can enlarge the pore connections and thus increase the permeability. In the current experiments, the permeability is doubled at 600 °C with a 1% increase in steel fiber volume fraction.

Fig. 3(a) illustrates a comparison between the model results and the experimental data, demonstrating an excellent match. To account for the initial decrease effect, the ratios of crack opening over ITZ thickness and crack water permeability over matrix permeability in Eq. (22) were properly reduced. The measured porosity in Step 1 is used to address the increasing effect of the permeability with the temperature as label in Fig. 2. This agreement confirms the validity of the proposed model's assumptions.

3.3. Influence of PP fiber content on plain concrete

This study examines the impact of PP fibers on concrete permeability after exposure to high temperatures. Two different dosages of PP fibers, S0P1L12 (0.1% volume fraction) and S0P2L12 (0.2% volume fraction), with a length of 12 mm, were tested. The results, shown in Fig. 4(a), indicate that the permeability of concrete increases with temperature and reaches a value $10^3 \sim 10^4$ times higher than the initial value at 20 °C when exposed to 600 °C. This variation is similar to SFRC behavior, where thermal cracking from

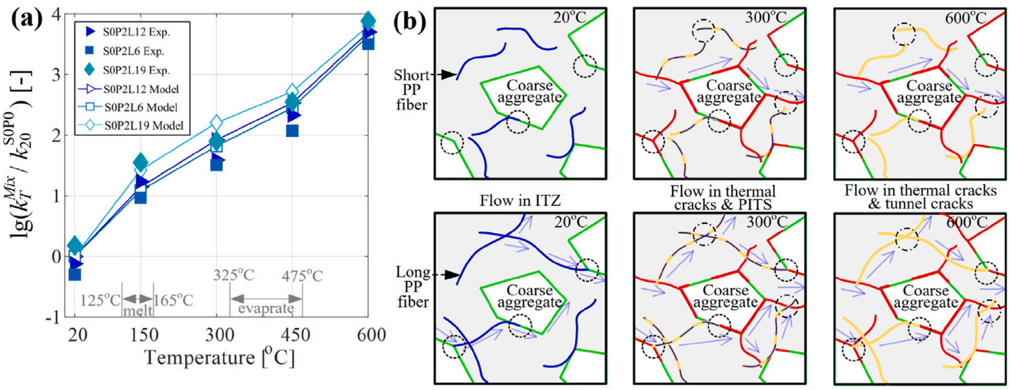

Fig. 5. Influence of PP fibers length: (a) experimental data and model predictions; (b) illustrations of meso-scale mechanisms.

coarse aggregate increases permeability above 300 °C, instead of tunnel cracks caused by PP fiber evaporation. The experimental measurements and model predictions (Eq. (25) with $V_{SF} = 0$) for S0P0, S0P1L12, and S0P2L12 are presented in Fig. 4(a).

When we compare the permeability of PFRCs at different temperatures, we can see that it decreases with the increase in the volume fraction of PP fibers at 20 °C. However, it increases with the increase in the volume fraction of PP fibers above 150 °C. This phenomenon is due to the physical and chemical reactions of PP fibers at different temperatures. At temperatures below 100 °C, PP fibers act as impermeable inclusions in the matrix. Thus, even a slight increase in the volume fraction of 0.1% can cause a small decrease in permeability.

Fig. 4(a) reveals a significant difference in permeability at 150 °C, which marks the starting point of PP fibers' melting and pore pressure build-up. The PP fibers undergo an endothermic melting phase starting at 125 °C [52], reaching its peak at 165 °C and fully melting at 176 °C. The melting process destroys the PP fibers' crystallinity, resulting in a wholly amorphous polymer [52,53]. The damage to the weak fiber–matrix interface occurs due to rising pore pressure, which allows vapor migration in the space created by poor interfacial contact rupture. This process is known as the Pressure-Induced Tangential Space (PITS) [52,54]. The addition of PP fiber results in a different evolution trend compared to the permeability decrease at 150 °C of plain concrete (S0P0). This is because, in PFRC, the effect of PITS at 150 °C associated with the Fiber Adhering Effect (FAE) [31,52] increases the connectivity of voids (pores and thermal cracks). This generates a mass transport network that allows steam to travel along this space at the beginning of PP fiber melting at 125 °C, resulting in the permeability of PFRC being 10^1 to 10^2 times higher than that of plain concrete at 150 °C. This phenomenon is the most relevant mechanism that increases the PFRC's permeability and releases concrete vapor pressure during heating. The PFRC's permeability increment in the temperature range from 100 °C to 300 °C is primarily determined by the combined effect of thermal cracking, PITS, and FAE.

As the temperature rises, PP fibers undergo vaporization at 325 °C, with the peak of vaporization occurring at around 460 °C and completing at 475 °C. This process involves breaking down the carbon backbone into smaller molecules through endothermic pyrolysis [52,53]. Following this, tunnel-like voids arise in the positions where fine PP fibers were present, creating continuous channels for moisture-vapor migration, particularly in connection to thermal cracks [52,54]. As a result, permeability increases by $2 \sim 5$ times at high temperatures.

In Fig. 4, it can be observed that PFRC and plain concrete have similar permeability values at temperatures above 300 °C. This is because the dominant mechanism affecting permeability changes from PITS and FAE to thermal cracks caused by coarse aggregates. At 450 °C, PFRC has a smaller permeability than plain concrete, which can be attributed to the fine-PP fibers that help reduce damage from pore pressure build-up. This explanation is indirectly supported by the porosity data presented in Table 2.

In Fig. 4(a), the results of the model and experimental data show good agreement. The PP fibers are considered impermeable inclusions below a temperature of 100 °C, and their volume fraction decreases with temperature due to melting and evaporation, as shown in Eq. (25) in Step 4. The measured porosity takes into account tunnel-type voids, as explained in Step 1. Furthermore, Eq. (8) in Step 1 accounts for the improved connectivity of pores through tunnel-type voids. The effect of thermal cracking and PITS caused by FAE is calculated using the term r_{FAE} in Eq. (22) in Step 2. By producing accurate predictions, the proposed model supports the reasonableness of our assumptions.

3.4. Influence of PP fiber length on plain concrete

We tested three PFRC mixes with varying lengths of PP fibers to see how the length affected concrete permeability after exposure to high temperatures. The results showed that all three mixes had increased permeability at 600 °C, with little impact from the length of the fibers. The results of the experiments and model predictions (using Eq. (25) with $V_{SF} = 0$) are shown in Fig. 5(a). The permeability of all three PFRC mixes increased with temperature and reached a value $5 \times 10^3 \sim 10^4$ times higher than the initial value at 600 °C.

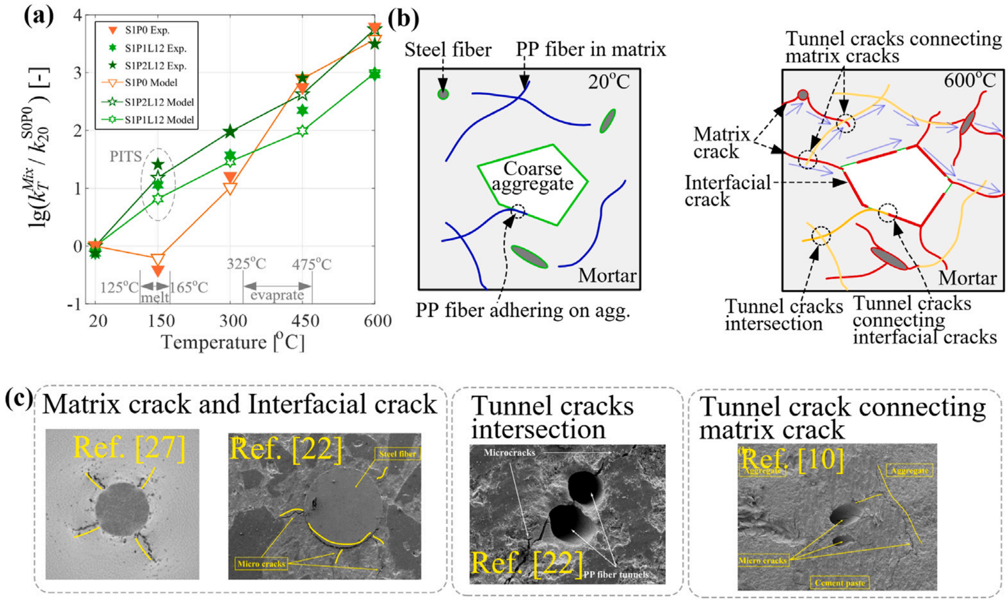

Fig. 6. Influence of PP fibers content on HSPFRC: (a) experimental data and model predictions; (b) illustrations of meso-structure; (c) Experimental evidence for the thermal crack patterns from [10,24,29].

In this discussion, we will explore the impact of PP fibers length on thermal cracking, PITS, and FAE. Out of all these effects, FAE appears to be the most significant factor. When the constituent materials in the mix remain constant, longer PP fibers tend to adhere more to the ITZ of coarse aggregates.[8,10,24]. After heat treatments, the likelihood of thermal cracks connecting increases with the length of PP fibers, leading to higher permeability, as depicted in Fig. 5(b). The smaller pore pressure peaks in concrete with longer PP fiber can be fully explained by the permeability increment [8,52,55].

According to Fig. 5(a), the proposed model takes into account two mechanisms that accurately replicate the experimental data. The increase in FAE due to the longer PP fibers is taken into account by the relationship between the fiber length and the term r_{FAE} in Eq. (22) (see Step 2). Additionally, the enhancement of pore connectivity resulting from the longer PP fibers is accounted for by the term $\beta(T, V_{PE}, L_{PF})$ in Eq. (8) (see Step 1).

3.5. Influence of PP fibers content on HSPFRC

We use two mixes of HSPFRC with fixed PP fiber length (12 mm) to study the combined effect of steel and fine PP fibers on permeability evolution during heating. The mixes we tested were S1P1L12 (1% steel fibers and 0.1% PP fibers by volume) and S1P2L12 (1% steel fibers and 0.2% PP fibers by volume). We compared the experimental data and model predictions for these mixes with the results of S1P0 in Fig. 6(a). As the temperature increased, the permeability of all three PFRCs also increased and reached a value of $10^3 \sim 10^4$ times the initial value at 600 °C. Adding 0.1% PP fibers significantly increases the permeability at 150 °C, and a further 0.1% increase in PP fibers slightly increases the permeability at all temperatures.

In Section 3.2 and Section 3.3, it was discussed that steel fibers and fine PP fibers have opposing effects on the permeability of concrete when exposed to temperatures ranging from 150 °C up to 300 °C. As illustrated in Fig. 6(b), adding steel fibers reduces permeability by preventing thermal cracks caused by coarse aggregates. In contrast, adding PP fibers increases permeability due to PITS and FAE. The pieces of evidence for the thermal cracking patterns are displayed in Fig. 6(c), including the numerical simulations of matrix and interfacial cracks [29,31], the tunnel cracks intersections [10], and the tunnel cracks-matrix cracks intersections [24]. The data in Fig. 6(a) indicate a more significant impact from fine PP fibers. This finding justifies the use of a combination of high- and low-melting-point fibers for anti-spalling concrete, as stated in [52].

When the temperature rises above 450 °C, both HSPFRC mixes, and S1P0 have the same permeability value. However, S1P1L12 has lower permeability than S1P0, while S1P2L12 has slightly higher permeability than S1P0. This suggests that thermal cracks from coarse aggregates affect the main water mass transport network. Additionally, tunnel-type voids and FAE connections improve the connectivity of transport networks in HSPFRC. However, the porosity of HSPFRCs does not vary significantly (refer to Table 2).

In Fig. 3, we have compared the model results with the experimental data. It is worth noting that we have used parameters identified from our calculations in Section 3.2 to Section 3.4. The fact that the model predictions match the experimental data shows that our proposed model is correct, precise, accurate, and reliable.

3.6. Influence of PP fibers length on HSPFRC

We tested three different mixtures with varying lengths of PP fibers and a fixed content of 0.2% of PP fibers and 1% of steel fibers in volume. The purpose of the test was to investigate the influence of fine PP fiber length on the permeability of HSPFRC

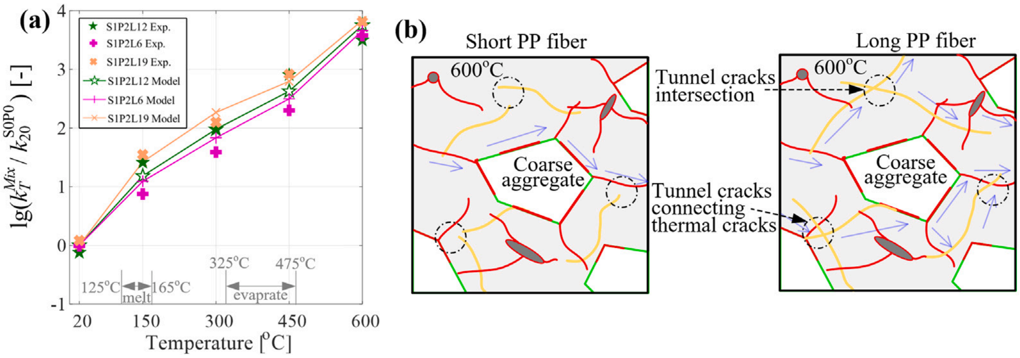

Fig. 7. Influence of PP fibers content on HSPFRC. (a) Experimental data and model predictions; (b)illustrations of meso-structure.

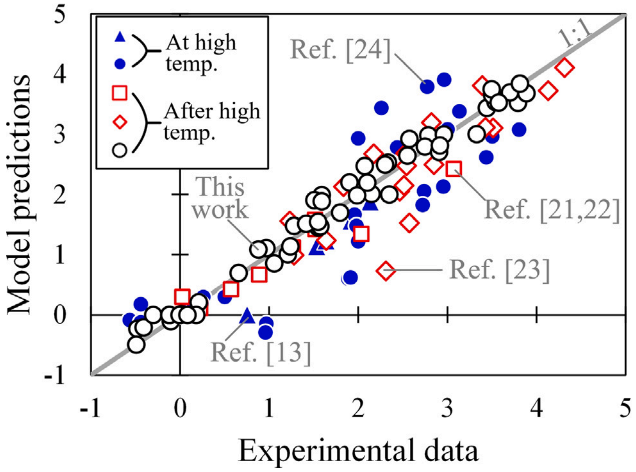

Fig. 8. Validation of the multiscale cracking pattern based homogenization model of HSPFRC permeability at/after high temperature.

after exposure to high temperatures. Fig. 7(a) shows the experimental measurements and model predictions (Eq. (25)) for the three mixes: S1P2L6 (PP fibers of 6 mm length), S1P2L12 (PP fibers of 12 mm length), and S1P2L19 (PP fibers of 19 mm length). We found that the permeability of HSPFRC increases with temperature and reaches a value of $5 \times 10^3 \sim 10^4$ times the initial value at 600 °C. Similar to PFRC, we observed that increasing the length of PP fibers can slightly increase the permeability value of HSPFRC.

As discussed in Fig. 6, the water movement in thermally damaged HSPFRC is facilitated by the thermal cracks that are created by the coarse aggregates and the steel fibers, as well as the PITS or tunnel-type voids that are formed when PP fibers evaporate. These pathways can be more effectively connected through the longer PP fibers depicted in Fig. 7(b). This can increase the likelihood of interfacial thermal cracks between the coarse aggregates (FAE) and other thermal cracks and voids. This deduction is supported by pore pressure measurements, which show that the peaks decrease as the length of PP fiber increases in HSPFRC [52].

According to the data shown in Fig. 5(a), the model's predictions closely match the experimental results and accurately reflect the impact of PP fiber length. Furthermore, all the necessary parameters for these calculations have already been identified in previous sections. The agreement between the model's predictions and experimental data confirms that it can effectively replicate the permeability of HSPFRC under different fiber lengths and heating temperatures.

4. Model validation

We validate the proposed model by comparing it with available experimental data from literature [13,21–24]. The experimental data on the permeability of HSPFRC are the residual permeability after exposure to high temperatures ranging from 80 °C to 500 °C, as reported in Table 4. Additionally, the hot permeability measured at high temperatures ranging from 20 °C to 300 °C and reported in Table 5 is also considered. As the porosity data are only available in [21,22], we use the porosity data measured in this work for the permeability predictions with our proposed model. All the permeability data, whether from literature or this work, are compared in the relative form of $\log_{10}(\kappa_T^{mix}/\kappa_{20}^{plain})$ or $\log_{10}(k_T^{mix}/k_{20}^{plain})$, as shown in Fig. 8. Our model predictions align well with the hot and residual permeability of concrete composites with coarse aggregates [13,21–23]. The model also exhibits the same trend for the hot permeability of UHPC (maximum aggregate is 600 μm).

Table 4
Permeability of HSPFRC after high temperature in literature.

Mix	Temp.		PP fibers			Steel fibers			Permeability	Ref.
		d_{max}	d_{PF}	L_{PF}	V_{PF}	d_{SF}	L_{SF}	V_{SF}	$\kappa \times 10^{-18}$ m^2	
	°C	mm	μm	mm	%	mm	mm	%	$k \times 10^{-12}$ m/s	
Plain	80	10			0			0	45	[21,22]
	200	10			0			0	59	
	300	10			0			0	180	
	500	10			0			0	1200	
CS	80	10			0	0.38	30	0.82	29	
	200	10			0	0.38	30	0.82	58	
	300	10			0	0.38	30	0.82	380	
	500	10			0	0.38	30	0.82	1100	
CPPS	80	10	32	12	0.77	0.38	30	0.82	45	
	200	10	32	12	0.77	0.38	30	0.82	210	
	300	10	32	12	0.77	0.38	30	0.82	920	
	500	10	32	12	0.77	0.38	30	0.82	1200	
Plain	80	10			0			0	2.5	[23]
	200	10			0			0	47.5	
	400	10			0			0	42.5	
P6-0.25	80	10	60	6	0.25			0	3.8	
	200	10	60	6	0.25			0	171	
	400	10	60	6	0.25			0	870.2	
P6-0.5	80	10	60	6	0.5			0	15.5	
	200	10	60	6	0.5			0	372	
	400	10	60	6	0.5			0	8122	
P30-0.25	80	10	60	6	0.25			0	14	
	200	10	60	6	0.25			0	1652	
	400	10	60	6	0.25			0	33 684	
P30-0.5	80	10	60	6	0.5			0	17.9	
	200	10	60	6	0.5			0	6157.6	
	400	10	60	6	0.5			0	51 480.4	
S30-0.5	80	10			0	0.6	30	0.25	22.2	
	200	10			0	0.6	30	0.25	510.6	
	400	10			0	0.6	30	0.25	932.4	
S30-0.5	80	10			0	0.6	30	0.5	5.2	
	200	10			0	0.6	30	0.5	109.2	
	400	10			0	0.6	30	0.5	728	
HY-A	80	10	60	6	0.25	0.6	30	0.5	68.1	
	200	10	60	6	0.25	0.6	30	0.5	817.2	
	400	10	60	6	0.25	0.6	30	0.5	1770.6	
HY-B	80	10	60	6	0.5	0.6	30	0.25	5.7	
	200	10	60	6	0.5	0.6	30	0.25	849.3	
	400	10	60	6	0.5	0.6	30	0.25	6657.6	

5. Conclusions

The use of hybrid steel-fine polypropylene (PP) fiber-reinforced concrete (HSPFRC) can be effective in preventing thermal spalling at high temperatures. This study aimed to provide more information on the mix design of HSPFRC by examining its permeability variation after exposure to high temperatures. The research team also proposed a multiscale homogenization model to predict HSPFRC permeability with inputs of porosities and mix information.

The study makes two significant contributions. Firstly, the research team conducted experiments using cylindrical specimens that were 200 mm long in the flow direction. This length is over three times the maximum diameter of the coarse aggregate, steel fiber length, and PP fiber length. This approach allowed for measuring a representative volume of the material, containing more comprehensive mesoscopic information than that found in the literature. Secondly, the analytical model is developed based on the mesoscopic crack pattern, including the porosity and pore connectivity, thermal cracks, PP fiber melting and evaporation, and PP fiber adhering to coarse aggregate (FAE). The model can accurately predict concrete permeability with different fiber types, contents, and sizes and with different high-temperature treatments. The model's accuracy is demonstrated by its excellent agreement with the experimental data not only from the presented investigation but also from the available literature.

In addition to the comprehensive experimental data, the multiscale cracking pattern-based homogenization model provides new insights into the mechanisms generating HSPFRC's high-temperature permeability variation, as in the following.

(a) Permeability increases up to 10^4 times between 20 °C and 600 °C due to interfacial thermal cracks caused by the expansion of coarse aggregates.
(b) Below 300 °C, the addition of 1% volume fraction of steel fiber can reduce the permeability of SFRCs by 10 times. This reduction occurs due to the impermeability of steel fiber and the bridging forces, which enhance the internal cohesion of the

Table 5
Permeability of SFRC and PFRC at high temperature in literature.

Mix	Temp.		PP fibers			Steel fibers			Permeability	Ref.
		d_{max}	d_{PF}	L_{PF}	V_{PF}	d_{SF}	L_{SF}	V_{SF}	$\kappa \times 10^{-18}$ m^2	
	°C	mm	μm	mm	%	mm	mm	%	$k \times 10^{-12}$ m/s	
Plain:	20	0.6			0			0	2.6	[24]
UHPC	100	0.6			0			0	3.2	
	150	0.6			0			0	10.2	
	200	0.6			0			0	85.3	
	250	0.6			0			0	103.7	
	300	0.6			0			0	765.0	
UHPC-PP	20	0.6	50	12	0.33			0	2.0	
	100	0.6	50	12	0.33			0	4.2	
	150	0.6	50	12	0.33			0	111	
	200	0.6	50	12	0.33			0	190	
	250	0.6	50	12	0.33			0	800	
	300	0.6	50	12	0.33			0	1010	
UHPC-S	20	0.6			0	0.22	13	2.5	1.4	
	100	0.6			0	0.22	13	2.5	2.8	
	150	0.6			0	0.22	13	2.5	10	
	200	0.6			0	0.22	13	2.5	92	
	250	0.6			0	0.22	13	2.5	114	
	300	0.6			0	0.22	13	2.5	753	
UHPC-AG	20	5			0			0	1.2	
	100	5			0			0	2.9	
	150	5			0			0	105	
	200	5			0			0	300	
	250	5			0			0	1100	
	300	5			0			0	1500	
UHPC-PPAG	20	5	50	12	0.33			0	1.5	
	100	5	50	12	0.33			0	1.6	
	150	5	50	12	0.33			0	998	
	200	5	50	12	0.33			0	3000	
	250	5	50	12	0.33			0	4100	
	300	5	50	12	0.33			0	6700	
Plain:	20	8						0	1.8	[13]
C80/95-PF0	80	8						0	2.0	
	150	8						0	10.0	
	200	8						0	60.0	
	300	8						0	250.0	
C80/95-PF1	20	8	15.4	6	0.11			0	2.0	
	80	8	15.4	6	0.11			0	2.2	
	140	8	15.4	6	0.11			0	76.8	
	150	8	15.4	6	0.11			0	146.7	
	170	8	15.4	6	0.11			0	240.0	
	200	8	15.4	6	0.11			0	633.3	

material. However, this increase in cohesion can also lead to higher pore pressure within the SFRCs, which can increase the risk of spalling.

(c) At 150 °C, the permeability of PFRCs increases by a factor of 10^2. An increase in both the content and length of PP fibers results in a corresponding increase in permeability. This phenomenon can be attributed to two factors, namely the Fiber Adhering Effect (FAE) and the Process Induced Thermal Strain (PITS). The FAE explains how longer PP fibers lead to better connectivity between thermal cracks.

(d) Regarding HSPFRCs, the permeability shows similar patterns to PFRCs. At 150 °C, the permeability of HSPFRCs containing 1% steel fibers is enhanced by over 10^2 times when 0.1% of PP fibers are added. This finding is indicative of the fact that the positive impact of fine PP fibers outweighs the negative impact of steel fibers, resulting in an overall increase in permeability.

For a more convenient way to predict permeability, a model of porosity for HSPFRC after high temperature would be developed based on thermal cracking patterns. This is something that will be developed in the future as development of the proposed approach.

CRediT authorship contribution statement

Lei Shen: Writing – review & editing, Writing – original draft, Visualization, Validation, Methodology, Investigation, Funding acquisition, Data curation, Conceptualization. **Li Zhang:** Writing – original draft, Validation, Investigation, Data curation. **Xiang Yang:** Writing – review & editing, Writing – original draft, Investigation, Formal analysis, Data curation. **Giovanni Di Luzio:** Writing – review & editing, Writing – original draft, Validation, Methodology, Investigation, Conceptualization. **Lei Xu:** Writing – review & editing, Supervision, Methodology, Funding acquisition. **Huimin Wang:** Validation, Investigation, Funding acquisition, Data curation. **Maosen Cao:** Writing – review & editing, Supervision, Methodology, Funding acquisition, Conceptualization.

Declaration of competing interest

The authors declare that they have no known competing financial interests or personal relationships that could have appeared to influence the work reported in this paper.

Data availability

Data will be made available on request.

Acknowledgments

The research presented in this paper was supported by Young Elite Scientists Sponsorship Program by Jiangsu Provincial Association for Science and Technology (TJ-2023-043), the National Natural Science Foundation of China (42202286, 52250410359), and the Jiangsu International Joint Research and Development Program, China (BZ2022010).

References

[1] Lei Shen, Weixin Li, Xinwei Zhou, Jun Feng, Giovanni Di Luzio, Qingwen Ren, Gianluca Cusatis, Multiphysics lattice discrete particle model for the simulation of concrete thermal spalling, Cem. Concr. Compos. 106 (2020) 103457.
[2] Lei Shen, Francesco Lo Monte, Giovanni Di Luzio, Gianluca Cusatis, Weixin Li, Roberto Felicetti, Federico Lombardi, Maurizio Lualdi, Maosen Cao, Qingwen Ren, On the moisture migration of concrete subject to high temperature with different heating rates, Cem. Concr. Res. 146 (2021) 106492.
[3] D. Gawin, F. Pesavento, B.A. Schrefler, Towards prediction of the thermal spalling risk through a multi-phase porous media model of concrete, Comput. Methods Appl. Mech. Engrg. 195 (41–43) (2006) 5707–5729.
[4] Jean-Christophe Mindeguia, Pierre Pimienta, Albert Noumowé, Mulumba Kanema, Temperature, pore pressure and mass variation of concrete subjected to high temperature. Experimental and numerical discussion on spalling risk, Cem. Concr. Res. 40 (3) (2010) 477–487.
[5] Francesco Lo Monte, Roberto Felicetti, Chiara Rossino, Fire spalling sensitivity of high-performance concrete in heated slabs under biaxial compressive loading, Mater. Struct. 52 (1) (2019) 14.1–14.11.
[6] S. Cattaneo, L. Biolzi, Assessment of thermal damage in hybrid fiber-reinforced concrete, J. Mater. Civ. Eng. 22 (9) (2010) 836–845.
[7] L. Shen, G. Di Luzio, D. Zhu, X. Yao, G. Cusatis, M. Cao, Y. Han, Y. Wang, Q. Ren, Mechanical responses of steel fiber-reinforced concrete after exposure to high temperature: Experiments and mesoscale discrete modeling, J. Eng. Mech. (11) (2021) 147.
[8] Pierre Kalifa, Grégoire Chéné, Christophe Gallé, High-temperature behaviour of HPC with polypropylene fibres: From spalling to microstructure, Cem. Concr. Res. 31 (10) (2001) 1487–1499.
[9] Jean Christophe Mindeguia, Helene Carre, P. Pimienta, C. La Borderie, Experimental discussion on the mechanisms behind the fire spalling of concrete, Fire Mater. 39 (7) (2015) 619–635.
[10] Y. Li, Y. Zhang, E.H. Yang, K.H. Tan, Effects of geometry and fraction of polypropylene fibers on permeability of ultra-high performance concrete after heat exposure, Cem. Concr. Res. 116 (2019) 168–178.
[11] F. Lo Monte, F. Lombardi, R. Felicetti, M. Lualdi, Ground-penetrating radar monitoring of concrete at high temperature, Constr. Build. Mater. (2017).
[12] Nizar Faisal Alkayem, Lei Shen, Ali Mayya, Panagiotis G. Asteris, Ronghua Fu, Giovanni Di Luzio, Alfred Strauss, Maosen Cao, Prediction of concrete and FRC properties at high temperature using machine and deep learning: A review of recent advances and future perspectives, J. Build. Eng. 83 (2024) 108369.
[13] J. Bošnjak, J. Ožbolt, R. Hahn, Permeability measurement on high strength concrete without and with polypropylene fibers at elevated temperatures using a new test setup, Cem. Concr. Res. 53 (2013) 104–111.
[14] J. Lee, K. Terada, M. Yamazaki, K. Harada, Impact of melting and burnout of polypropylene fibre on air permeability and mechanical properties of high-strength concrete, Fire Saf. J. 91 (jul.) (2017) 553–560.
[15] Dong Zhang, Kang Hai Tan, Effect of various polymer fibers on spalling mitigation of ultra-high performance concrete at high temperature, Cem. Concr. Compos. 114 (2020) 103815.
[16] A.N. Noumowe, R. Siddique, G. Debicki, Permeability of high-performance concrete subjected to elevated temperature (600 °c), Constr. Build. Mater. 23 (5) (2009) 1855–1861.
[17] Ghasem Pachideh, Majid Gholhaki, An experimental study on the effects of adding steel and polypropylene fibers to concrete on its resistance after different temperatures, J. Test. Eval. 47 (2019) 20170145.
[18] Ghasem Pachideh, Majid Gholhaki, Amin Moshtagh, Performance of concrete containing recycled springs in the post-fire conditions, Proc. Inst. Civ. Eng. - Struct. Build. 173 (2018) 1–38.
[19] Ghasem Pachideh, Majid Gholhaki, Using steel and polypropylene fibres to improve the performance of concrete sleepers, Proc. Inst. Civ. Eng. - Struct. Build. 173 (2019) 1–38.
[20] Ghasem Pachideh, Hesam Ketabdari, Investigation of the mechanical properties of self-compacting concrete containing recycled steel springs; Experimental and numerical investigation, Eur. J. Environ. Civ. Eng. 27 (2023) 1–20.
[21] N. Algourdin, P. Pliya, A.L. Beaucour, A. Simon, A Noumow, Influence of polypropylene and steel fibres on thermal spalling and physical-mechanical properties of concrete under different heating rates, Constr. Build. Mater. 259 (6) (2020) 119690.
[22] N Yermak, P Pliya, A.L Beaucour, A Simon, A Noumowe, Influence of steel and/or polypropylene fibres on the behaviour of concrete at high temperature: Spalling, transfer and mechanical properties, Constr. Build. Mater. 132 (FEB.1) (2017) 240–250.
[23] S.L. Suhaendi, T. Horiguchi, Effect of short fibers on residual permeability and mechanical properties of hybrid fibre reinforced high strength concrete after heat exposition, Cem. Concr. Res. 36 (9) (2006) 1672–1678.
[24] Ye Li, Kang Hai Tan, En-Hua Yang, Influence of aggregate size and inclusion of polypropylene and steel fibers on the hot permeability of ultra-high performance concrete (UHPC) at elevated temperature, Constr. Build. Mater. 169 (2018) 629–637.
[25] S.C. ASTM, Standard test method for flow of hydraulic cement mortar, ASTM (2007).
[26] Crack effects on gas and water permeability of concretes, Cem. Concr. Res. 39 (6) (2009) 537–547.
[27] S.D. Abyaneh, H.S. Wong, N.R. Buenfeld, Simulating the effect of microcracks on the diffusivity and permeability of concrete using a three-dimensional model, Comput. Mater. Sci. 119 (2016) 130–143.
[28] Xiuli Du, Liu Jin, Renbo Zhang, Yue Li, Effect of cracks on concrete diffusivity: A meso-scale numerical study, Ocean Eng. 108 (2015) 539–551.
[29] Y.F. Fu, Y.L. Wong, C.A. Tang, C.S. Poon, Thermal induced stress and associated cracking in cement-based composite at elevated temperatures Part I: Thermal cracking around single inclusion, Cem. Concr. Compos. 26 (2) (2004) 99–111.

[30] Y.F Fu, Y.L Wong, C.A Tang, C.S Poon, Thermal induced stress and associated cracking in cement-based composite at elevated temperatures part II: thermal cracking around multiple inclusions, Cem. Concr. Compos. 26 (2) (2004) 113–126.

[31] Lei Shen, Giovanni Di Luzio, Maosen Cao, Qingwen Ren, Xuhua Ren, Mingkai Jiang, De Zhu, Xiupeng Yao, Insights and theoretical model of thermal conductivity of thermally damaged hybrid steel-fine polypropylene fiber-reinforced concrete, Cem. Concr. Compos. 138 (2023) 105001.

[32] Qiannan Wang, Guoshuai Zhang, Yunyun Tong, Chunping Gu, Prediction on permeability of engineered cementitious composites, Crystals 11 (5) (2021).

[33] Lu Cui, Jong Herman Cahyadi, Permeability and pore structure of OPC paste, Cem. Concr. Res. 31 (2) (2001) 277–282.

[34] B.H. Oh, S.Y. Jang, Prediction of diffusivity of concrete based on simple analytic equations, Cem. Concr. Res. (3) (2004) 463–480.

[35] Hassan Baji, Chun-Qing Li, An analytical solution for hydraulic conductivity of concrete considering properties of the interfacial transition zone (ITZ), Cem. Concr. Compos. 91 (2018) 1–10.

[36] Hassan Baji, Wei Yang, Chun-Qing Li, Wenhai Shi, Analytical models for effective hydraulic sorptivity, diffusivity and conductivity of concrete with interfacial transition zone, Constr. Build. Mater. 225 (2019) 555–568.

[37] Gaurav Sant, Dale Bentz, Jason Weiss, Capillary porosity depercolation in cement-based materials: Measurement techniques and factors which influence their interpretation, Cem. Concr. Res. 41 (8) (2011) 854–864.

[38] Armin Jamali, Joao Mendes, Brabha Nagaratnam, Michael Lim, A new four stage model of capillary pressure in early age concrete: Insights from high capacity tensiometers, Cem. Concr. Res. 161 (2022) 106955.

[39] Enrico Masoero, Gianluca Cusatis, Giovanni Di Luzio, C–S–H gel densification: The impact of the nanoscale on self-desiccation and sorption isotherms, Cem. Concr. Res. 109 (2018) 103–119.

[40] A.J. Katz, A.H. Thompson, Quantitative prediction of permeability in porous rock, Phys. Rev. B 34 (1986) 8179–8181.

[41] G.F. Peng, Z.S. Huang, Change in microstructure of hardened cement paste subjected to elevated temperatures, Constr. Build. Mater. 22 (4) (2008) 593–599.

[42] T.C. Powers, Structure and physical properties of hardened Portland cement paste, 41(1), 1958, pp. 1–6.

[43] Torben C. Hansen, Physical structure of hardened cement paste. a classical approach, Mater. Struct. 19 (6) (1986) 423–436.

[44] D.P. Bentz, E.J. Garboczi, Percolation of phases in a three-dimensional cement paste microstructural model, Cem. Concr. Res. (1991).

[45] Dariusz Gawin, Francesco Pesavento, Bernhard A. Schrefler, What physical phenomena can be neglected when modelling concrete at high temperature? A comparative study. Part 1: Physical phenomena and mathematical model, Int. J. Solids Struct. 48 (13) (2011) 1927–1944.

[46] Hui Wang, Xi Chen, Sha Yang, Antonio Caggiano, Qing Ai, Eduardus Koenders, Yong Yuan, A dehydration kinetic model of calcium silicate hydrates at high temperature, Struct. Concrete 24 (2) (2023) 1997–2008.

[47] Andreas Stumm, Krassimir Garbev, Günter Beuchle, Leon Black, Peter Stemmermann, Rolf Nüesch, Incorporation of zinc into calcium silicate hydrates, part I: formation of C-S-H(I) with C/S=2/3 and its isochemical counterpart gyrolite, Cem. Concr. Res. 35 (9) (2005) 1665–1675.

[48] Jintao He, Dong Lei, Giovanni Di Luzio, Feipeng Zhu, Pengxiang Bai, Mechanical properties measurement and micro-damage characterization of ITZ in concrete by SEM-DIC method, Opt. Lasers Eng. 155 (2022) 107064.

[49] Z. Hashin, Thin interphase/imperfect interface in conduction, J. Appl. Phys. 89 (2001) 2261–2267.

[50] H. Fricke, A mathematical treatment of the electric conductivity and capacity of disperse systems. I. The electric conductivity and capacity of disperse systems, Phys. Rev. 24 (1924) 106–115.

[51] R.L. Hamilton, O.K. Crosser, Thermal conductivity of heterogeneous two-component systems, Ind. Eng. Chem. Fundam. 1 (3) (1962) 187–191.

[52] Lei Shen, Xiupeng Yao, Giovanni Di Luzio, Mingkai Jiang, Yang Han, Mix optimization of hybrid steel and polypropylene fiber-reinforced concrete for anti-thermal spalling, J. Build. Eng. 63 (2023) 105409.

[53] G.A. Khoury, B. Willoughby, Polypropylene fibres in heated concrete. Part 1: Molecular structure and materials behaviour, Mag. Concr. Res. 60 (2) (2008) 125–136.

[54] G.A. Khoury, Polypropylene fibres in heated concrete. Part 2: Pressure relief mechanisms and modelling criteria, Mag. Concr. Res. 60 (3) (2008) 189–204.

[55] Mugume Rodgers Bangi, Takashi Horiguchi, Effect of fibre type and geometry on maximum pore pressures in fibre-reinforced high strength concrete at elevated temperatures, Cem. Concr. Res. 42 (2) (2012) 459–466.